infrastructures

MDPI

Article

Experimental and Numerical Study on Local Buckling Analysis of Q550 High-Strength Steel T-Rib-Stiffened Plates

Peng Chen [1], Qingtian Su [1], Yongcheng Lu [2,*], Sizhe Wang [3] and Yanhong Chen [1]

[1] College of Civil Engineering, Tongji University, Shanghai 200092, China; sqt@tongji.edu.cn (Q.S.); 2510459@tongji.edu.cn (Y.C.)
[2] Shanghai Municipal Engineering Design Institute (Group) Co., Ltd., Shanghai 200092, China
[3] Singapore Centre for 3D Printing, Nanyang Technological University, Singapore 639798, Singapore; sizhe.wang@ntu.edu.sg
* Correspondence: luyongcheng@smedi.com; Tel.: +86-17721180501

Abstract

In high-strength steel structures, local plate buckling is a critical concern due to the slenderness of plate elements. This study experimentally and numerically investigated the local buckling analysis of Q550 high-strength steel stiffened plates with T-ribs under compression. Five specimens with different base-plate slenderness were fabricated and subjected to uniaxial compression loading tests. The base plate of all specimens exhibited significant local out-of-plane deformation, and the T-ribs experienced varying degrees of in-plane and out-of-plane deformations. The buckling strength of the specimens decreases with increasing base-plate slenderness. The residual stresses and initial geometric imperfections of the high-strength steel stiffened plate were experimentally measured. Finite element (FE) models incorporating the residual stresses and initial geometric imperfections were established to simulate the buckling behavior of the stiffened plates. The FE models were validated against the experimental results and a parametric study was further conducted. The numerical results indicate that both residual stresses and initial geometric imperfections have a moderate influence on the buckling strength. Furthermore, the formulations in several national design codes used to account for local buckling effects were evaluated. The Eurocode provides approximate predictions, while the Chinese code and Japanese code provide conservative estimations.

Keywords: high-strength steel; local buckling behavior; stiffened plate; initial geometric imperfection; residual stress; design code

Check for updates

Academic Editor: Fabrizio Scozzese

Received: 5 June 2026
Revised: 9 July 2026
Accepted: 16 July 2026
Published: 20 July 2026

Copyright: © 2026 by the authors. Licensee MDPI, Basel, Switzerland. This article is an open access article distributed under the terms and conditions of the Creative Commons Attribution (CC BY) license.

1. Introduction

Steel structures are widely adopted in modern engineering due to their high strength-to-weight ratio, excellent ductility, and reliable seismic performance. Their prefabrication capability, rapid construction, and recyclability further enhance economic and environmental sustainability. Steel stiffened plates, which consist of a base plate and ribs, are effective and economical systems commonly used in steel structures, for example, serving as fundamental components in welded steel box girders, arches, and towers of steel bridges [1–3]. As thin-walled structural components, steel stiffened plates are prone to instability-induced failure when they are subjected to high compressive loads. This instability may manifest in several modes, including local buckling of the base plate between ribs, local buckling of the ribs, overall column-type buckling of the stiffened plate, as well as other possible buckling modes, significantly reducing structural resistance and stiffness [4].

From the 1950s onward, with the increasing use of welded stiffened plates in large steel structures, research attention shifted toward the buckling behavior of plate–stiffener systems [5]. At the same time, the influence of residual stresses and initial geometric imperfections began to receive systematic attention. Residual stresses arising from welding and fabrication were recognized as an important factor affecting plate stability. Initial geometric imperfections, such as out-of-plane plate deflections and stiffener misalignments, were also identified as critical parameters governing buckling behavior. From the 1970s to the 1990s, the accumulation of experimental data enabled the development of simplified design-oriented buckling models that implicitly account for residual stresses and initial geometric imperfections [6–9]. The corresponding research results were adopted by multiple national codes, and design provisions for the local buckling of plates in these codes were continuously optimized [10–12].

In recent years, high-strength steel (HSS), defined as steel with a yield strength of not less than 460 MPa, has attracted increasing attention from both practical engineers and academic researchers, and its usage in contemporary steel construction has become an important design option [13–15]. The drive for the efficient use of HSS demands structural components to be designed in a reasonable way to achieve its merits in economy and safety when compared with conventional mild steel (CMS) [16–18]. In contrast with CMS structures, the steel plates are usually designed thinner in HSS structures. Although ribs enhance the overall buckling resistance of stiffened plates, the risk of local plate buckling increases with decreasing plate thickness. Hence, the plate local buckling behavior has become a specific critical issue for HSS structures. However, the existing research results on the local stability of stiffened plates are mostly focused on CMS. The current Chinese specification for the design of highway steel bridges is only applicable to steel with a yield strength of up to 420 MPa [10]. The current Eurocode for the design of steel bridges extrapolates the application scope to steels with a yield strength of 690 MPa [19]. Nevertheless, the Eurocode design method for evaluating the stability resistance of axially compressed members was primarily developed for CMS structures, and its applicability to HSS structures remains questionable, which may not fully balance the safety and cost-effectiveness of HSS structures due to the differences in material properties between CMS and HSS [18,20,21]. Therefore, it is necessary to conduct a comprehensive study on the local buckling behavior of high-strength steel stiffened plates.

In practical bridge engineering, stiffeners in stiffened plates come in various forms, categorized as closed ribs and open ribs. Closed ribs mainly include trapezoidal and U-shaped cross-sections with high torsional stiffness, excellent stability, and high material utilization, effectively preventing buckling [22,23]. However, their complex weld connections and difficulties in internal corrosion prevention and inspection limit their application range to some extent, especially in steel arches and towers. Open ribs mainly include flat plates, T-sections, angles, and bulb flats, are easy to connect, inspect, and maintain, and have a wider range of applications [10,19]. Under axial compression, a stiffened plate equipped with T-ribs exhibits a stronger restraint against local plate buckling than plates stiffened with other types of open ribs. Chou et al. [24] carried out axial compression tests on T-rib-stiffened plates fabricated from Q345 steel, and pointed out that the Japanese codes overly conservatively underestimate the buckling performance of stiffened plates. Choi et al. [25] further conducted tests on the ultimate load-bearing capacity of the T-rib-stiffened plates, and verified that T-ribs possess superior buckling resistance compared with other open rib stiffened plates. Sadamoto et al. [26] analyzed various buckling failure modes of T-rib-stiffened plates. Preliminary research on high-strength steel stiffened plates has been reported in the existing literature [27], which revealed that current design codes tend to give overly conservative predictions for the buckling behavior of stiffened plates.

This study investigates the local buckling behavior of the base plate of high-strength steel stiffened plates under compression. Stiffened plate specimens with T-ribs made of high-strength steel with a yield strength grade of 550 MPa (Q550) were fabricated for uniaxial compression tests. The residual stresses of the high-strength steel stiffened plate were experimentally measured through the destructive sectioning method. Finite element (FE) models with residual stresses and geometric imperfections taken into consideration were established and validated by the experiment. Based on the validated FE models, a parametric analysis was performed to investigate the influence of residual stresses, geometric imperfections and boundary conditions on the buckling behavior. Finally, the design formula in various national codes accounting for the local buckling behavior of stiffened plates was evaluated.

2. Experimental Program

2.1. Material Properties

This study investigated T-rib-stiffened plates fabricated with Q550 high-strength steel (i.e., having a yield strength $\geq$ 550 MPa). The material properties of the employed Q550 steel were measured through tensile coupon tests. The stiffened plate specimens (as introduced in the following subsection) were made of Q550 steel plates with thicknesses of 6 mm and 8 mm, and the corresponding stress–strain curves are presented in Figure 1. The average measured values of the key mechanical properties, including the Young's modulus E, the yield strength f_y, the ultimate strength f_u, the strain at the end of the yield plateau ε_{sh}, and the strain at the ultimate strength ε_u, are summarized in Table 1. The actual yield strengths of the 6 mm and 8 mm steel plates were 15.1% and 12.7% higher than the specified yield strength (550 MPa).

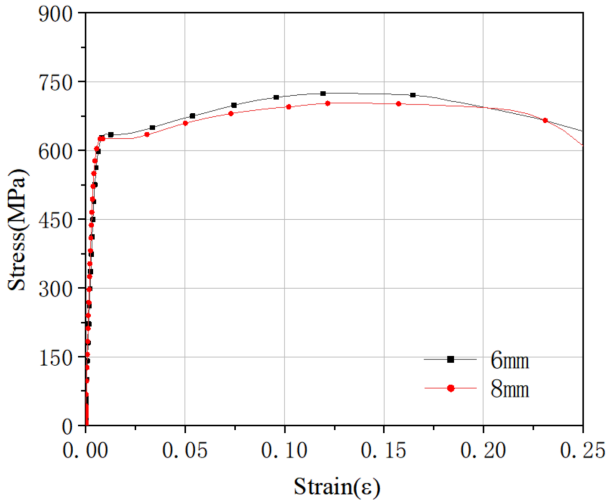


Figure 1. Stress–strain curves of Q550 steel.

Table 1. Average measured material properties of Q550 steel.

Steel Grade	Thickness	E	f_y	f_u	ε_{sh}	ε_u
Q550	6	206	633	722	0.014	0.107
	8	203	620	702	0.017	0.111

2.2. Specimen Design

Stiffened plates with three T-ribs, as shown in Figure 2, were designed as specimens for uniaxial compression tests and their respective dimensional parameters are listed in Table 2. The experimental program included residual stress measurements, initial

geometric imperfection measurements and uniaxial compression tests, as detailed in the following subsections.

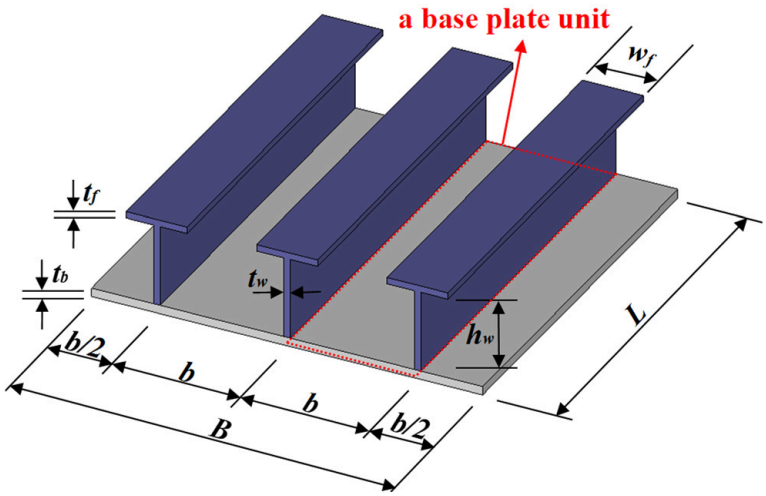


Figure 2. 3D sketch of stiffened plate specimens for uniaxial compression tests.

Table 2. Specimen dimensional parameters.

Specimen	Test *	Size of Base Plate (mm)				Plate Slenderness of Base Plate Unit		Size of T-rib (mm)				Total Area(mm^2)
		L	*B*	*b*	t_b	Nominal	True	h_w	t_w	w_f	t_f	
S04	UCT	360	360	120	8	0.40	0.44	75	6	56	6	5454
S07	UCT	630	630	210		0.70	0.76					7614
S10	UCT	900	900	300		1.01	1.09					9774
S13	UCT	1170	1170	390		1.31	1.42					11,934
S16	UCT	1440	1440	480		1.61	1.74					14,094
RS16	RSM	2880	960	480		1.61	1.74					9396

* UCT: uniaxial compression tests. RSM: residual stress measurements.

The dimensions of the specimens for uniaxial compression tests were specifically designed as follows. The plate slenderness $\overline{\lambda}_p$, calculated via Equation (1) cited from design codes, represents the critical parameter governing plate buckling strength [10–12]. Based on the nominal yield strength of Q550 steel (550 MPa), the plate slenderness of the base plate unit (hereafter referred to as the base-plate slenderness) was designed as 0.4, 0.7, 1.0, 1.3, and 1.6 (corresponding to the nominal values in Table 2) for investigating the effect of plate slenderness.

$$\overline{\lambda}_p = \left(\frac{b}{t}\right)\sqrt{\frac{12(1-\mu^2)f_y}{kE\pi^2}} \quad (1)$$

where b and t are the width and thickness of plates; μ is Poisson's ratio; E is the Young's modulus; k denotes the buckling coefficient and is assigned a value of 4.0, as the stiffeners are designed with sufficient rigidity; and f_y is the yield strength.

As the local buckling of the base plate in the high-strength steel stiffened plate was the primary focus of this study, the dimensions of the T-ribs were intentionally designed to satisfy the requirements for rigid ribs according to the design code [10]. Therefore, the stiffened plate was divided into several base plate units by rigid ribs. The spacing b between adjacent stiffeners served as the width of the base plate, and the thickness t_b of the stiffened plate was taken as the thickness of the base plate. The specimen length L was set to three times the base plate width, so as to guarantee identical aspect ratios and enable the target local buckling to occur. The T-rib flange-to-web joints and the T-rib-to-base plate

joints were fillet-welded with a nominal leg size of 6 mm. Notably, the cross-sectional area of fillet-welded was incorporated into the total cross-sectional area *A*.

As shown in Table 2, a total of five stiffened plate specimens for uniaxial compression tests were fabricated. The label for each specimen (e.g., S04) consists of the letter "S" to denote the abbreviation of "stiffened plate" and the number (e.g., 04) to denote the nominal base-plate slenderness (e.g., 0.40). Based on the measured material properties of Q550 steel listed in Table 1, the true base-plate slenderness of each stiffened plate specimen was computed and presented in Table 2.

2.3. Residual Stress Measurements

Residual stresses are predominantly caused by the heat imparted to the plate along a weld, typically fillet welds of attached ribs [28,29]. The rapid heating of the separate parts and subsequent cooling of the welded assembly introduces a tensile stress zone close to the weld which is balanced by compressive stress zones away from the weld.

The destructive sectioning method is widely used in residual stress measurements for steel members [1]. To examine the residual stress distribution of the specimens, a stiffened plate specimen RS16, as plotted in Figure 3a, was prepared for destructive sectioning. The specimen RS16 with two T-ribs can be regarded as the stiffened plate shown in Figure 2 with a T-rib and a base plate unit removed. The specimen was 960 mm wide and 2880 mm long, with all other dimensions identical to those of specimen S16, as shown in Table 2.

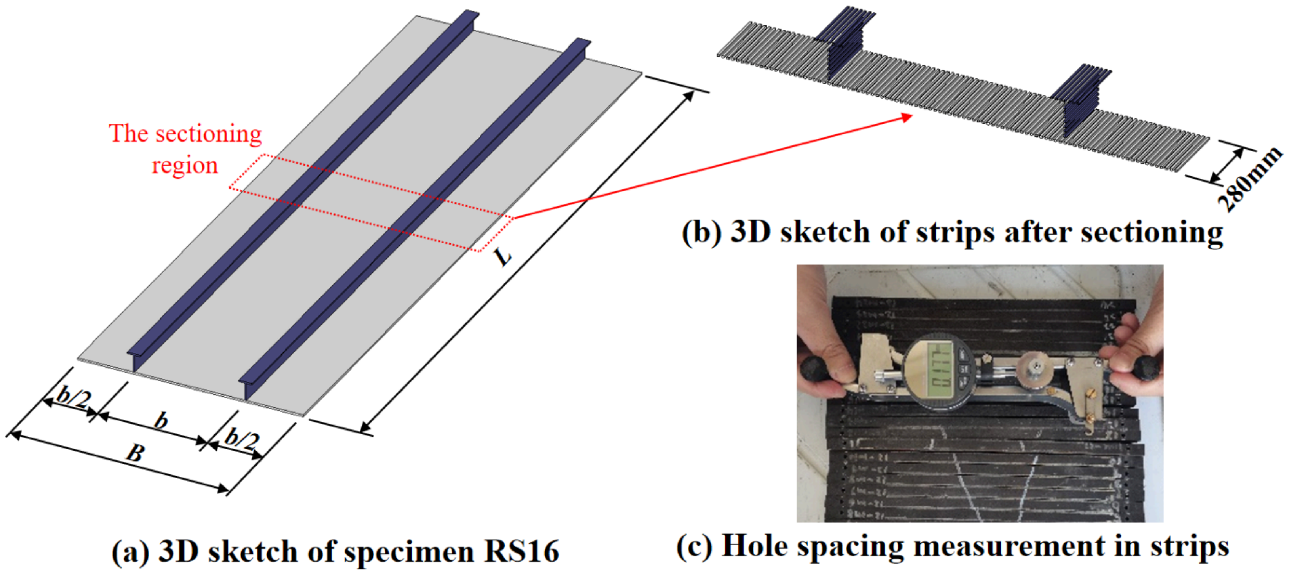


Figure 3. Residual stress measurements.

The sectioning region with a length of 280 mm was set in the middle and gauge holes were drilled with 250 mm longitudinal spacing. The strips with a width of approximately 10 mm were sectioned by a wire cutting machine. The actual hole distances were measured by YB-25 strain gauge before and after the cutting operation, as shown in Figure 3c. In addition, a reference strip was employed for temperature compensation. Notably, significant strip bending did not occur throughout testing, and geometric deformation effects were therefore neglected.

2.4. Initial Geometric Imperfection Measurements

Initial geometric imperfections are important factors affecting structural stability [23,30]. Thus, the initial geometric imperfections of the specimens, particularly the initial out-of-plane imperfections of the base plate, were carefully measured using a similar method

to that adopted in Refs. [1,31]. The initial geometric imperfections were quantified by establishing a reference plane using steel rulers and measuring the distance from the base plate surface to the reference plane with a digital depth gauge. The accuracy of the digital depth gauge was 0.01 mm. In practice, the measurement error was approximately ±0.05 mm, and its influence on the test results was negligible. Figure 4 shows the layout of the measurement points for the initial geometric imperfections.

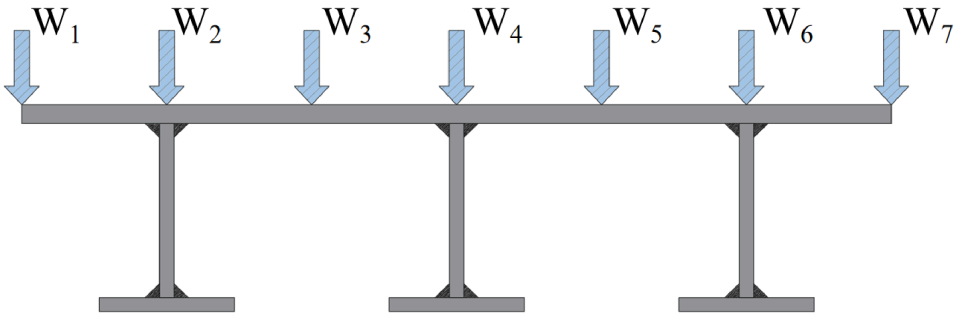


Figure 4. Measurement points for geometric imperfections layout.

As the local buckling of the base plate was likely to occur between adjacent T-ribs, the local buckling behavior was considered sensitive to the initial local imperfections of the base plate between adjacent T-ribs. Thus, the measurement points W_2 and W_6 are taken as the zero reference points. Table 3 records the initial geometric imperfections measurement results of specimens. The initial imperfections of all specimens primarily manifested as a protrusion on the base plate side. The imperfection amplitude-to-width (B) ratios were 1/325, 1/271, 1/203 and 1/314, and 1/236 for specimens S04 to S16, respectively.

Table 3. Measured local initial geometric defects of specimens.

Specimen	W_1	W_3	W_4	W_5	W_7	W_i-max/B
S5-120-04	−0.25	0.20	0.37	0.19	−0.26	1/325
S5-210-07	−0.51	0.51	0.77	0.48	−0.49	1/271
S5-300-10	−1.46	0.61	1.48	0.48	−1.17	1/203
S5-390-14	−0.81	0.55	1.24	0.42	−0.86	1/314
S5-480-17	−1.38	0.87	2.03	0.81	−1.54	1/236

2.5. Uniaxial Compression Tests

The loading setup for uniaxial compression tests is shown in Figure 5. The specimens were vertically placed and axially compressed in the testing machine with a loading capacity of 20,000 kN. To restrain translational displacement at both ends of the stiffened plate specimens during axial compression, two limiting plates with a groove and two bearing plates without a groove were designed to match each specimen, as shown in Figure 5c. The groove in the limiting plates was slightly larger than the cross-section of the corresponding specimen. The process of installing the specimens into the loading device was as follows: (1) two limiting plates were bolted to the bearing plates to form two double-layer plates; (2) both ends of each specimen were inserted into the grooves of the two double-layer plates; (3) the gaps between the grooves and the specimen were filled with small steel pieces; (4) the assembled specimen and double-layer plates were placed into the loading device. During the loading process, the double-layer plates ensured that the specimens were subjected to uniform compression without lateral movement. In addition, two angles were connected by bolts to clamp the base plate on each lateral side, ensuring that local buckling occurred first in the base plate between the T-ribs.

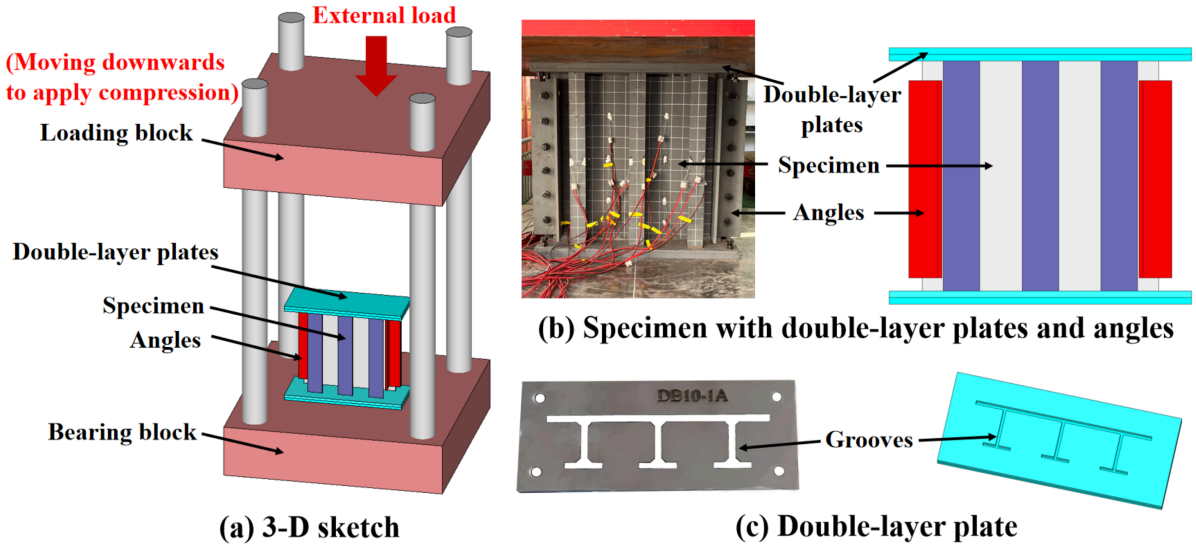


Figure 5. Loading setup for uniaxial compression tests.

The instrumentation for each specimen, comprising four linear variable differential transformers (LVDTs), is shown in Figure 6a. Four LVDTs were set up in the longitudinal direction to monitor the axial shortening of the specimens. Moreover, the strain gauges shown in Figure 6b were attached to the cross-sections of the specimens at the quarter points along the longitudinal direction, namely cross-sections N1, N2 and N3, to record the axial strain of the base plate. The strain gauges used are of type BX120-3AA.

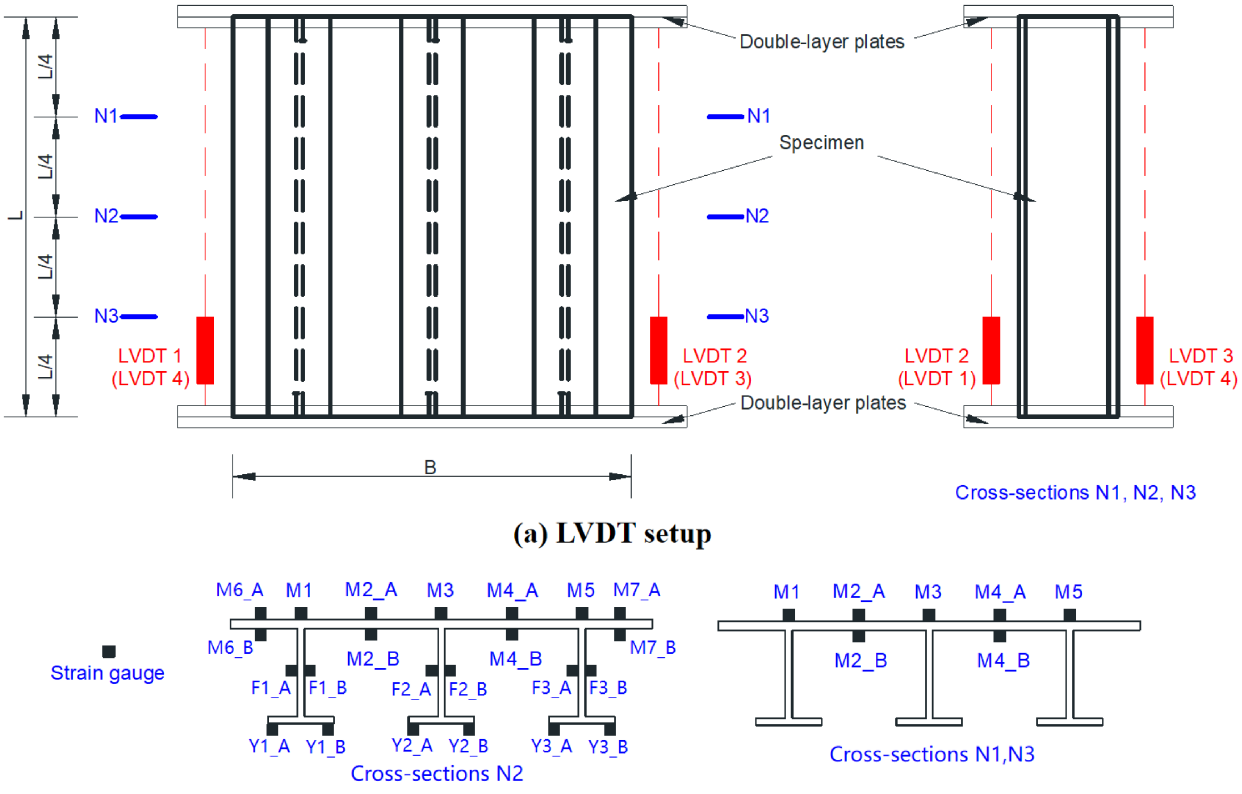


Figure 6. Instrumentation in uniaxial compression tests.

The pre-loading was carried out for each specimen to check the channels of the monitoring system, the alignment of the specimen, and to eliminate the gaps between

the loading device and the specimen. During the formal loading stage, a load-controlled loading protocol was adopted with a loading rate of approximately 2 kN/s. When the load value reached approximately 80% of the estimated bearing capacity of the specimens, or when minor local buckling deformation was observed in the base plate, loading was switched to displacement control at approximately 0.1 mm/min. The test was terminated when the load dropped to approximately 80% of the peak value or when pronounced buckling occurred in the specimens.

3. Experimental Results

3.1. Residual Stresses

Residual stresses were measured as described in Section 2.3, and the results from the two T-ribs and the corresponding base plate units were averaged to obtain the magnitude and distribution of longitudinal residual stresses across the cross-section, as shown in Figure 7a. A peak tensile stress of 548 MPa ($0.88\,f_y$) was observed near the weld on the base plate, while the average compressive stress between the ribs was approximately −50 MPa ($-0.08\,f_y$). In the T-rib flanges, the peak tensile stress reached 547 MPa ($0.88\,f_y$), similar to that in the base plate, whereas the peak compressive stress was −263 MPa ($-0.42\,f_y$). In the T-rib webs, the peak tensile and compressive stresses reached 493 MPa ($0.79\,f_y$) and −225 MPa ($-0.36\,f_y$), respectively. Based on the distribution model proposed in the reference [32–34], combined with the test results, a simplified model distribution was obtained, as shown in Figure 7b.

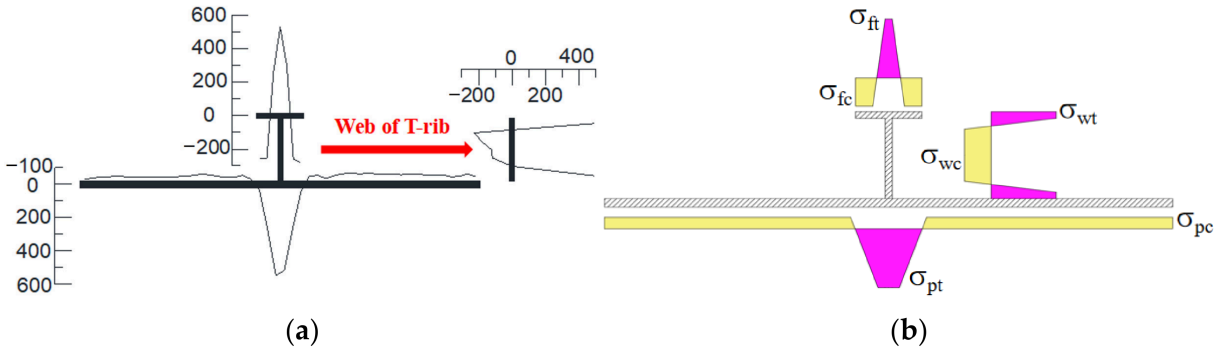


Figure 7. Residual stresses of stiffened plates. (**a**) Measured stresses (MPa). (**b**) Simplified model in Refs. [32–34].

3.2. Uniaxial Compression Test Results

3.2.1. Failure Modes

The failure modes of all specimens in the uniaxial compression tests are presented in Figure 8. Significant local out-of-plane deformation was observed in the base plate of the specimens, and the T-ribs exhibited varying degrees of in-plane and out-of-plane deformations, indicating interactive buckling characterized by coupled deformation between the base plate and the T-ribs. For specimens S07 to S16, a half-wave deformation pattern developed in the base plate between adjacent T-ribs, representing a buckling mode dominated by local buckling of the base plate. In contrast, for specimen S04 with the smallest base-plate slenderness, no such half-wave pattern was observed in the base plate between the T-ribs, and the T-ribs underwent pronounced flexural deformation along their full length, suggesting a buckling mode governed by plate–stiffener interaction.

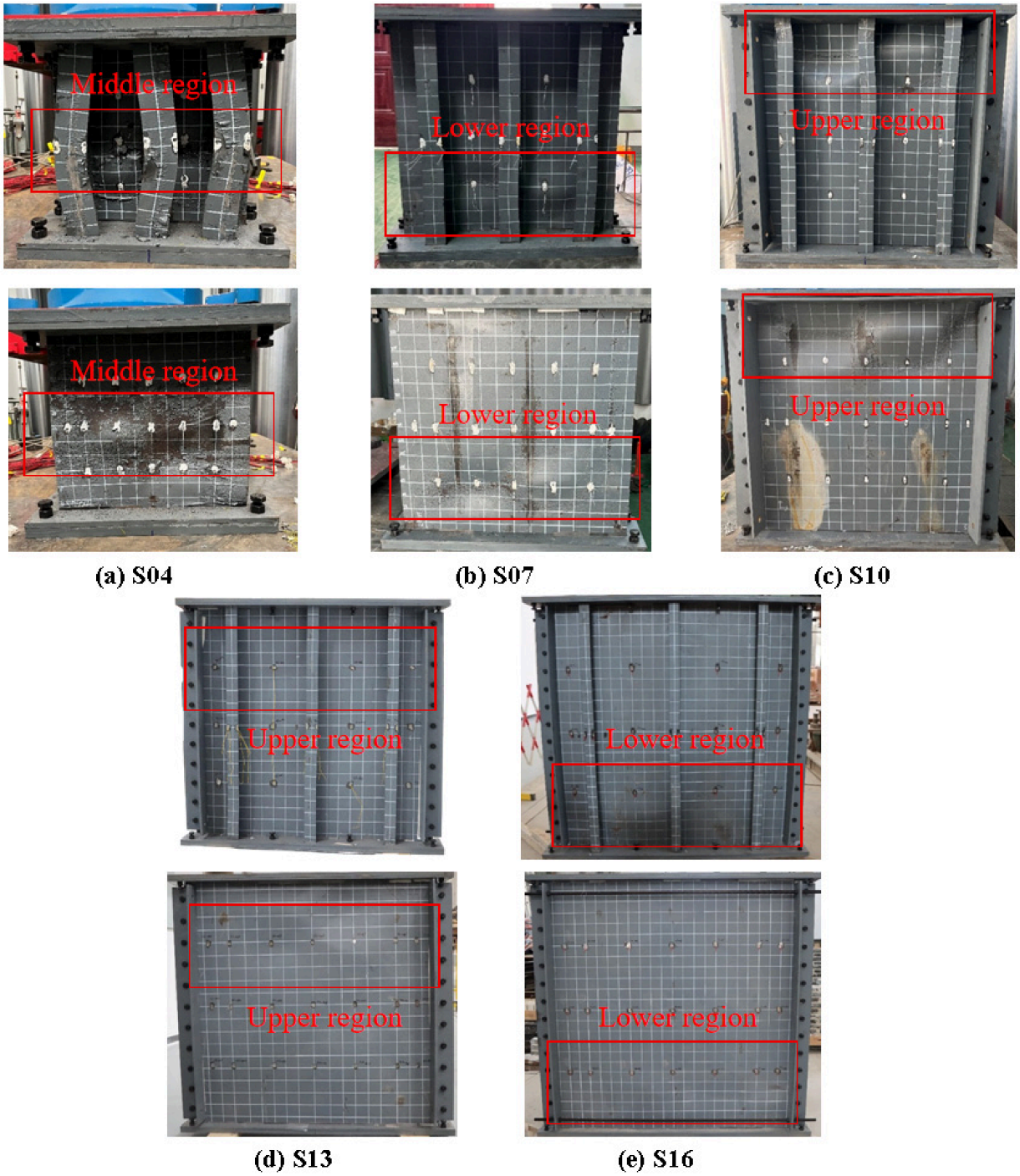


Figure 8. Failure modes of specimens in uniaxial compression tests.

The region of maximum local out-of-plane deformation differed among the specimens, occurring near mid-length of specimen S04, in the lower region of specimens S07 and S16, and in the upper region of specimens S10 and S13, which might be attributed to differences in initial imperfections and residual stresses. In addition, although steel pieces were used to fill the gaps between the grooves of the double-layer plates and the specimens, there were still some minor gaps after filling, which might also affect the location of maximum local out-of-plane deformation.

Note that the failure modes shown in Figure 8 correspond to the post-peak conditions and are influenced by the post-peak loading process. After the peak load was reached, the load decreased while deformation continued to increase; longer post-peak loading

resulted in more pronounced deformation. Nevertheless, the post-peak loading process did not affect the analysis of the buckling behavior (corresponding to the peak load). The base-plate deformations in specimens S13 and S16 were relatively limited compared with those in the other specimens, because loading was terminated shortly (earlier than for the other specimens) after the maximum load was reached for safety reasons.

The failure processes of all specimens were similar, and specimen S16 was taken as a representative example to illustrate the overall failure process. For specimen S16, when the applied load reached approximately 3800 kN (61.0% $P_{u\text{-}s16}$, where $P_{u\text{-}s16}$ denotes the bearing capacity of specimen S16), minor out-of-plane deformation of the base plate was observed near cross-section N3. When the load increased to 6226 kN ($P_{u\text{-}s16}$), both the amplitude and range of the out-of-plane deformation of the base plate increased, accompanied by minor deformation of the T-ribs. As the loading block of the loading device continued to move downward, the deformations of both the base plate and the T-ribs became progressively more pronounced, while the load decreased continuously.

Based on the loading process of all specimens, the failure development process of the specimens can be roughly divided into three stages. In Stage 1, the deformation remained visually unnoticeable as the load increased. In Stage 2, with further loading, minor out-of-plane deformation developed in the base plate. Upon reaching the ultimate load, the local deformation of the base plate intensified, accompanied by deformation of the T-ribs to varying extents. In Stage 3, the load decreased with increasing axial shortening, while the deformation of the base plate continued to evolve and the T-ribs exhibited varying degrees of in-plane and out-of-plane deformations.

3.2.2. Average Stress–Axial Shortening Relationship

To analyze whether the specimens yield under the peak load in the test, the load sustained by the specimens was divided by the cross-sectional area (including the fillet welds) to obtain the average stress of the cross-section. The average stress–axial shortening curves of all specimens are shown in Figure 9, and the buckling strengths of the stiffened plates are presented in Table 4. The buckling strength σ_b was defined as the ratio of the ultimate bearing capacity to the cross-sectional area.

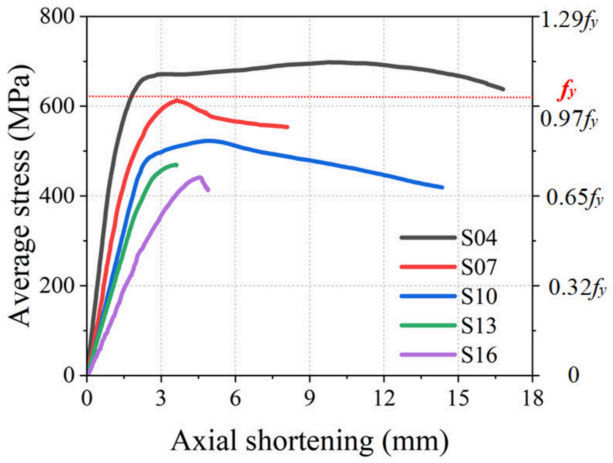


Figure 9. Average stress–axial shortening relationship in uniaxial compression tests.

The average stress–axial shortening curves of the specimens exhibit the same trend and can be divided into three stages, which correspond to the three stages of the specimen failure process described in Section 3.2.1. In Stage 1, as the load increased, the axial shortening increased almost linearly. In Stage 2, local out-of-plane deformation progressed, leading to a gradual reduction in axial stiffness until the peak load was reached. In Stage

3, the axial shortening continued to increase and the load gradually decreased (instead of dropping suddenly), with the specimens still possessing a substantial load-bearing capacity to resist the load. Note that the loading of specimens S13 and S16 was terminated shortly after the peak load was reached for safety concerns, and as such their post-peak curves were not obtained.

Table 4. Comparison of bearing capacities and buckling strengths.

Specimen	Bearing Capacity (kN)	Buckling Strength σ_b (MPa)	Yield Strength of the Base Plate f_y (MPa)	σ_b/f_y
S04	3806	698	624	111.9%
S07	4671	613		98.2%
S10	5112	523		83.8%
S13	5603	469		75.2
S16	6226	442		70.8%

When the load reached the ultimate bearing capacity, the average stress of specimen S04 exceeded the yield strength of the base plate, whereas the average stresses of the other specimens were lower than the yield strength. Table 4 shows that the buckling strength decreases with increasing base-plate slenderness, and specimen S16 exhibits the lowest buckling strength among all specimens, corresponding to 70.8% of the yield strength.

3.2.3. Average Stress–Axial Strain Relationship

The average stress–axial shortening relationship reflects the changes in the overall stiffness of the stiffened plate specimens under compression, while the average stress–axial strain relationship can clearly reflect the local out-of-plane deformation of the base plate. As shown in Figure 6, strain gauges were arranged on cross-sections N1, N2, and N3 of each specimen to monitor the axial strain. Based on the failure mode of each specimen shown in Figure 8, the average stress–axial strain curves are plotted according to the axial strain of the cross-section closest to the location with the most pronounced local out-of-plane deformation, as shown in Figure 10. For specimens S04, S07, S10, S13 and S16, the axial strains of base plate at cross-sections N1, N3, N2, N2 and N3 are presented, respectively.

For specimen S04 with the smallest base-plate slenderness, local out-of-plane deformation occurred in the base plate with full-section yielding, as shown in Figure 10a. In the initial stage of the test, the compressive strain distribution at various locations on the base plate was relatively uniform, indicating a state of uniform compression across the entire cross-section. As the load approached the peak value, local out-of-plane deformation occurred in the base plate, and the two surfaces of the base plate at this location were subjected to local tension and compression, respectively. The local tensile strain generated on the tension surface partially counteracted the axial compressive strain, resulting in a reduced strain growth rate of the base plate near the deformation region.

For specimens S07 to S16, which have relatively larger base-plate slenderness, the compressive strain distribution at different locations in the base plate was relatively uniform during the initial stage of the test. However, when local out-of-plane deformation occurred in the base plate, the average stress–axial strain curve showed a clear inflection point. Taking specimen S16 as a representative example, as shown in Figure 10e, during the initial loading stage, the specimen remained in the linear elastic range, and the compressive strain at each measuring point on cross-section N3 was uniformly distributed. When the average stress increased to approximately 235 MPa, the compressive strain values at measuring points N3-M2_B and N3-M4_A began to decrease, corresponding to a clear inflection point on the average stress–axial strain curves. The two measuring points on the back of the base

plate at the same location, measuring points N3-M2_A and N3-M4_B, showed opposite strain responses.

The average stress–axial strain responses of the specimens showed a similar trend. In the initial loading stage, the compressive strain distribution in the base plate was relatively uniform, indicating an approximately uniform compression state across the cross-section. With further increase in the average stress, local out-of-plane deformation developed in the base plate, leading to a rapid increase or decrease in axial compressive strain, and in some cases, a transition to tensile strain.

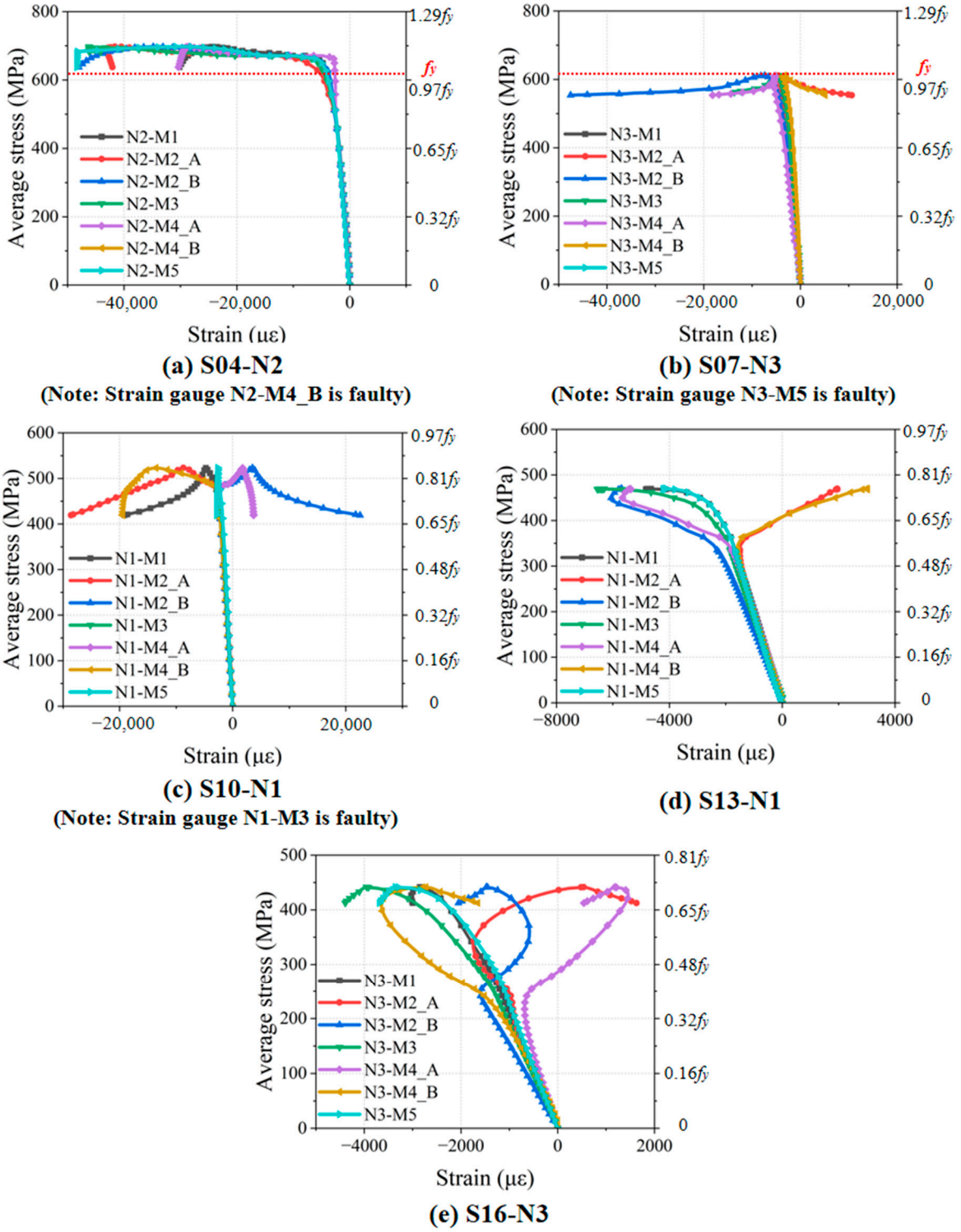


Figure 10. Average stress–axial strain relationship in uniaxial compression tests.

4. Numerical Analysis of Uniaxial Compression Tests

4.1. Finite Element Models

In conjunction with the experimental investigations, numerical analyses were performed to develop reliable FE models capable of reproducing the test results and providing deeper insight into the buckling behavior. Details of the numerical investigations are presented in this section.

FE models of the uniaxial compression tests were established in ABAQUS, as shown in Figure 11. In each FE model, the stiffened plate specimen including the fillet welds was built and meshed with the S4R element (i.e., a four-node shell element with reduced integration from the ABAQUS element library), which was successfully applied in previous numerical investigations of stiffened plate buckling [28,35]. The fillet welds were assumed to be symmetric and represented by two web elements with equal height but different widths (i.e., thicknesses), as illustrated in Figure 11 [36]. The global mesh was applied using a size of $b/20$ (b denotes the width of the base plate unit shown in Figure 2).

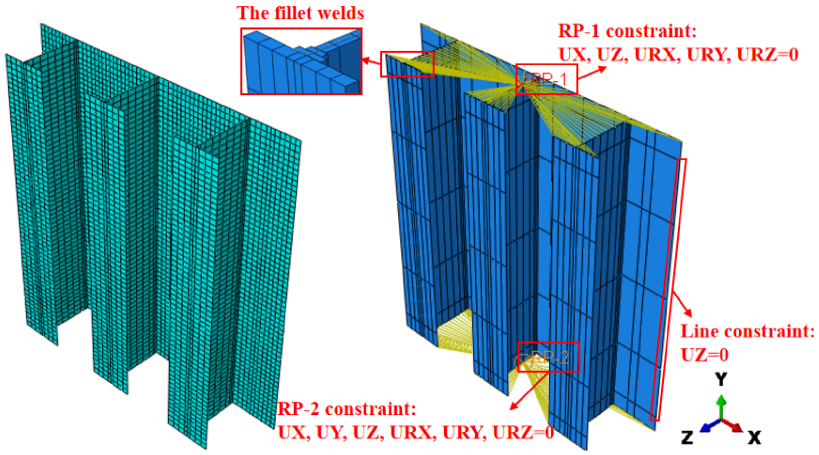


Figure 11. Finite element models.

With regard to the boundary conditions, each end cross-section of the stiffened plate specimens was coupled to a reference point, positioned on the centroid axis of the cross-section, by means of kinematic coupling constraints. Two reference points were denoted as RP-1 and RP-2, as shown in Figure 11. Since the ends of the stiffened plate specimens were constrained by two double-layer plates in the experiment, all translational and rotational degrees of freedom of RP-1 and RP-2 were constrained, except for the translational degree of freedom in the Y direction of RP-1. The uniaxial compression was applied to the stiffened plate specimens by applying the load at RP-1 in Y direction. In addition, the translational degree of freedom in Z direction of the nodes on the two side edges of the stiffened plate specimens was constrained to simulate the stiffening from angles, as described in Section 2.5, and the unconstrained lengths at the top and bottom ends of two side edges were 20 mm.

The multilinear kinematic hardening model plotted in Figure 12 was used as the constitutive model of both the base plate and the T-ribs, with the corresponding parameters listed in Table 1. The true stress–strain relationship was implemented in ABAQUS by converting the nominal stress and strain through Equations (2) and (3).

$$\sigma_{true} = \sigma_{norm}(1 + \varepsilon_{norm}) \tag{2}$$

$$\varepsilon_{true} = \ln(1 + \varepsilon_{norm}) \tag{3}$$

where σ_{true} and ε_{true} are true stress and strain; and σ_{norm} and ε_{norm} are nominal stress and strain.

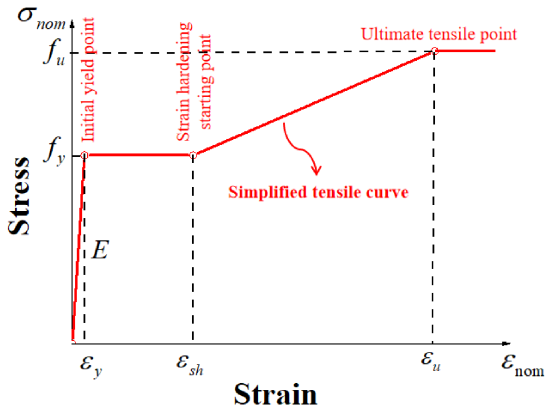


Figure 12. Multilinear kinematic hardening model.

Initial geometric imperfections and residual stresses were simulated simultaneously in each FE model. There are two commonly used methods for introducing initial geometric imperfections in FE models: (1) the superposition of buckling eigenmodes (hereinafter referred to as the Eigenmode method), (2) the direct translation of nodes (hereinafter referred to as the Translation method) [37]. The Translation method can introduce initial imperfections that are more in line with the actual situation. However, the Eigenmode method is easier and more generally applicable for introducing initial imperfections in FE models. Therefore, both methods for introducing initial imperfections in FE models were adopted and compared here. For the Eigenmode method, the first eigenmode obtained from modal analysis was used as the initial imperfection shape, and the imperfection amplitude was taken from the initial local imperfection amplitude "W_i-max/B" of the base plate shown in Table 3. For the Translation method, the initial imperfections recorded in Table 3 were directly imported into the FE models. Specimens S04 and S16 were selected as representative cases, and their first eigenmodes from the modal analysis were shown in Figure 13. The first eigenmodes exhibit a buckling mode dominated by local buckling of the base plate, accompanied by slight T-rib deformation. Figure 14 shows the result of introducing the initial imperfections into specimen S16 using the Translation method.

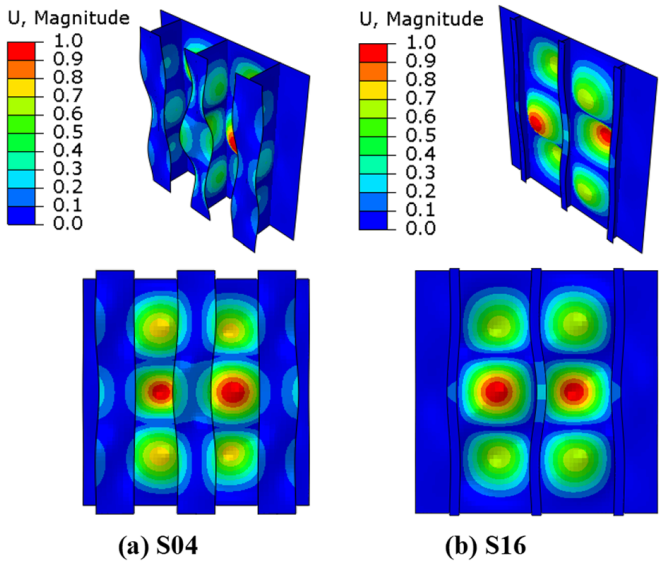


Figure 13. First eigenmode of specimens S04 and S16 (mm).



Figure 14. Initial imperfections of S16 imposed by Translation method.

The residual stress distribution in the base plate was assumed to follow the model shown in Figure 7b, as reported in Refs. [32–34]. While previous studies commonly assumed the peak tensile residual stress σ_t to be f_y, the measured value of 0.9 f_y was adopted in the present study. Based on the determined σ_t value, using the self-balancing principle and the literature, the residual compressive stress σ_c corresponding to different sizes of substrates can be calculated, thereby defining the residual stress distributions in the base plates of the specimens. In addition, the residual stress distributions in the T-ribs were taken from the measured results of the T-ribs in specimen RS16. These residual stresses were introduced as initial stresses in the elements of the FE models, and the resulting residual stress distribution for specimen S16 is shown in Figure 15.

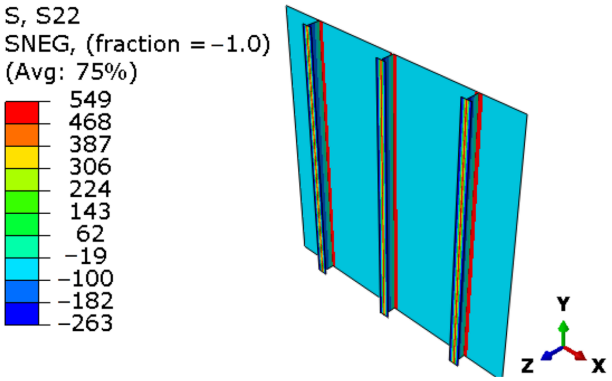


Figure 15. Residual stresses of specimen S16 (MPa).

4.2. Validation of Finite Element Models

4.2.1. Comparison of Failure Modes from Tests and FE Models

The five specimens in uniaxial compression tests were simulated. Two initial geometric imperfection introduction methods were employed for the simulation (due to incomplete initial geometric imperfection measurement data for specimen S04, it was only analyzed using the Eigenmode method, whereas specimens S07 to S16 were analyzed using both imperfection introduction methods).

Figure 16 shows the deformations at the true scale of the FE model for specimen S04 and the two FE models for specimen S16 under almost the same maximum loading displacement as in the tests. The deformation of specimen S04 in Figure 16a almost matches the actual failure mode shown in Figure 8a. The location of the maximum local deformation in specimen S16 in Figure 16b,c differs from that in Figure 8e; however, the failure mode is dominated by large local out-of-plan deformation of the base plate, consistent with the experimental results. A similar phenomenon was observed in the numerical simulations of specimens S07 to S13. This discrepancy might be attributed to differences between the actual boundary conditions in the experiments and the idealized boundary conditions assumed in the FE simulations. In the tests, the boundary conditions were realized using grooves in double-layer plates and small filling steel pieces. As a result, contact between components was not perfectly tight, with minor gaps in some regions and stress concentrations in others, such that the end constraints of the specimens could not be fully idealized. Consequently, noticeable local buckling in some specimens occurred near the top or bottom ends during the experiments.

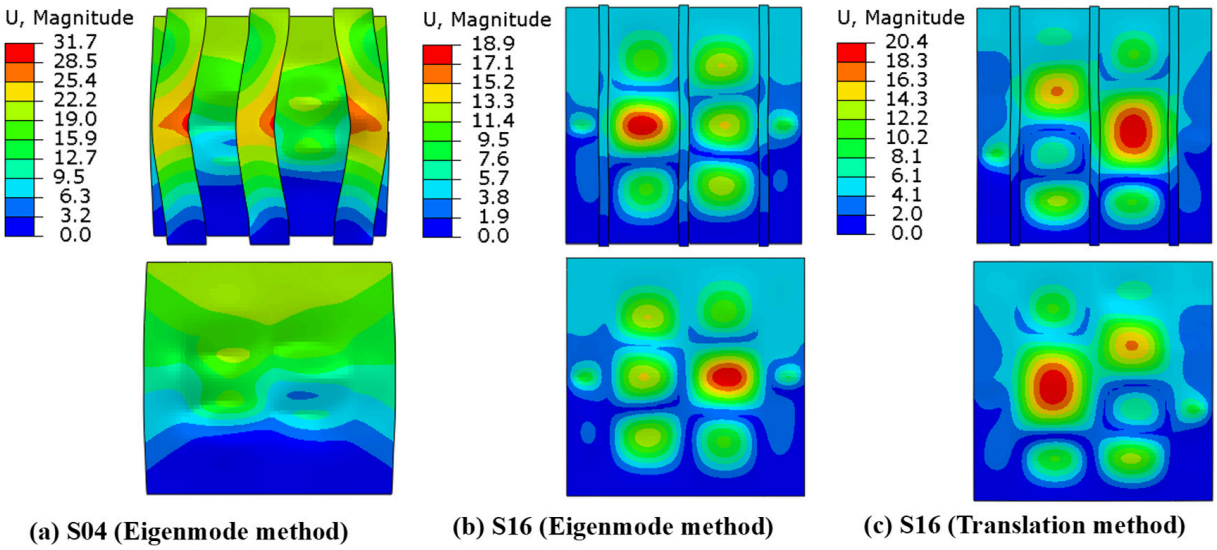


Figure 16. Deformations of specimens S04 and S16 from FE models (mm).

4.2.2. Comparison of Average Stress–Axial Shortening Curves from Tests and FE Models

The reaction of average stress to axial shortening of the specimens obtained from the FE models is plotted in Figure 17. It is clearly shown that the average stress–axial shortening curves agree reasonably well with test results, but the curves exhibit minor discrepancies at the ultimate stage. The corresponding buckling strengths of specimens from the tests and FE models are compared in Table 5. The discrepancy between the numerical and experimental buckling strengths of specimens is limited to 4.6%. As mentioned above, this difference may be due to factors such as the gaps between the specimens and the double-layer plates in the tests, which differ from the ideal conditions of the FE models.

Table 5. Comparison of buckling strengths from tests and FE models.

Specimen	Buckling Strength			$S_{FE\text{-}EM}/S_{Exp}-1$	$S_{FE\text{-}TM}/S_{Exp}-1$	$S_{FE\text{-}TM}/S_{FE\text{-}EM}-1$
	Experiment	FE Model (Eigenmode Method)	FE Model (Translation Method)			
	S_{Exp} (MPa)	$S_{FE\text{-}EM}$ (MPa)	$S_{FE\text{-}TM}$ (MPa)			
S04	698	666	/	−4.6%	/	/
S07	613	620	632	1.1%	3.0%	1.9%
S10	523	526	537	0.6%	2.7%	2.0%
S13	469	478	480	1.8%	2.3%	0.5%
S16	442	433	429	−2.0%	−2.9%	−0.9%

According to the simulation results of specimens S07 to S16, the average stress–axial shortening curves obtained from the FE models with initial imperfections introduced by the two methods are slightly different, and the difference in buckling strength is within 2.0%. This indicates that both methods are suitable for imposing initial imperfections on the FE models for simulating the buckling behavior of the specimens.

Consequently, by comparing the failure modes and buckling strengths of specimens from the test and simulation results, the FE models presented in Section 4.1 are able to predict the local buckling of the high-strength steel stiffened plate with T-ribs under compression.

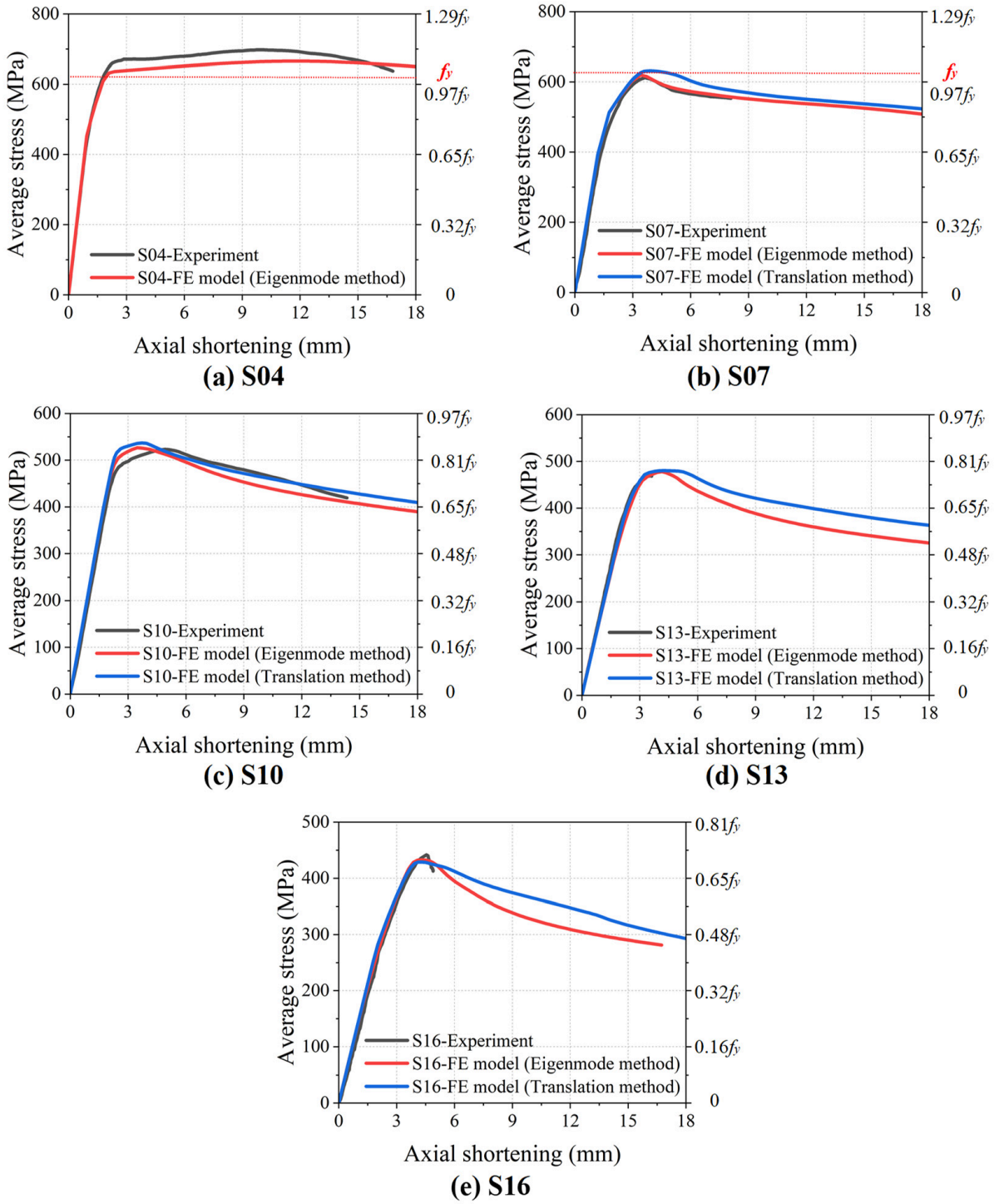


Figure 17. Average stress–axial shortening curves from tests and FE models.

4.3. Validation of Failure Modes

Figure 18 shows the out-of-plane deformations of specimens S04 and S16 at the peak load obtained from the validated FE analysis. The deformation mode of specimen S04 in Figure 18a differs from the first eigenmode shown in Figure 13a, whereas that of specimen S16 in Figure 18b is generally consistent with the first eigenmode in Figure 13b. This comparison provides evidence that the failure modes of specimens S07 to S16 are dominated by instability of the base plate between adjacent T-ribs, while specimen S04 exhibits a buckling mode governed by plate–stiffener interaction, as described in Section 3.2.1.

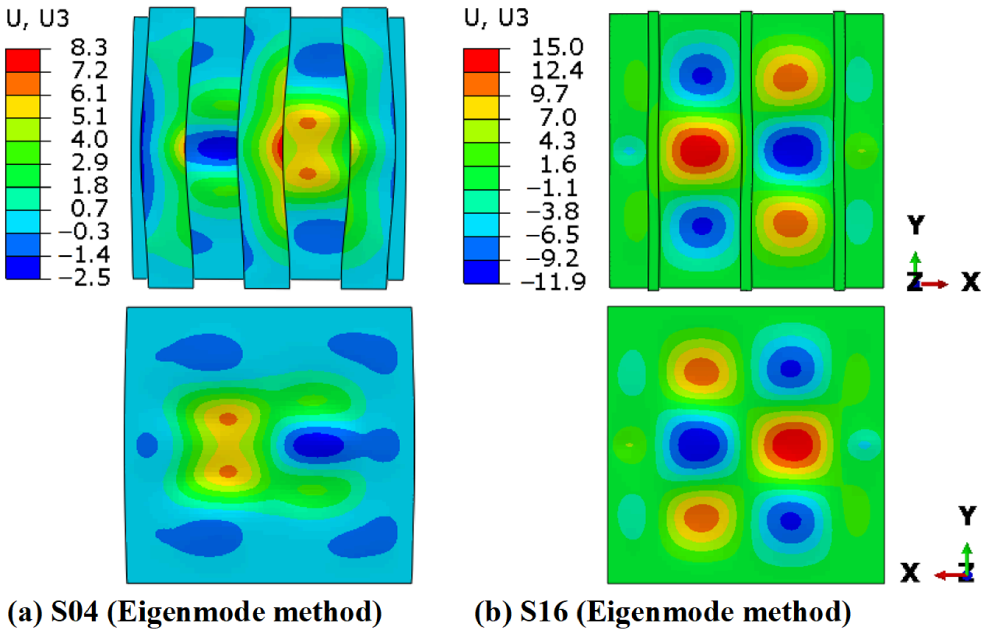


Figure 18. Out-of-plane deformations of specimens S04 and S16 from FE models (mm).

4.4. Parametric Analysis

Based on the verified FE models, a parametric study was carried out to discuss the influences on buckling behavior from three variables, including (1) initial geometric imperfections, (2) residual stresses, and (3) boundary conditions. Since the FE simulation results of introducing initial imperfections through the Eigenmode method and Translation method were slightly different as mentioned above, and the Eigenmode method was a simpler way to introduce initial imperfections, the Eigenmode method was adopted to introduce initial imperfections in parametric analysis. The first eigenmode of modal analysis was used as the initial imperfection shape. The base-plate slenderness of specimens S04 and S16 is the smallest and largest, respectively. Hence, the analysis was based on the FE models of these two specimens.

4.4.1. Effect of Initial Geometric Imperfections

As for the Eurocode, the initial imperfection amplitude of the base plate between the stiffening ribs of a box girder should be less than $b/125$, while the initial imperfection amplitude of the base plate between the stiffening ribs in a stiffened plate should be less than $b/250$ according to the Chinese code [38,39]. Therefore, the influence of these two imperfection amplitudes was analyzed. Furthermore, the residual stress distribution described in Section 4.1 was still adopted.

The parameters of the FE models used to analyze the influence of the initial imperfections are shown in Table 6. The average stress–axial shortening curves obtained from the simulations are plotted in Figure 19, illustrating that the introduction of initial imperfections leads the stiffened plate to reach its ultimate state at a smaller axial shortening, and the corresponding buckling strength is also reduced. Table 6 clearly shows that the initial imperfection amplitudes of $b/250$ and $b/125$ lead to a maximum reduction of 6.1% and 7.0% in the buckling strength, respectively. Hence, the buckling strength is moderately affected by the amplitude of initial geometric imperfections.

Table 6. Comparison of buckling strengths (effect of initial geometric imperfections).

FE Model	Initial Geometric Imperfection	Residual Stress	Buckling Strength (MPa)	Difference in Buckling Strength
S04_null_resi	null	As described in Section 4.1	675	/
S04_250_resi	$b/250$		666	−1.3%
S04_125_resi	$b/125$		654	−3.1%
S16_null_resi	null		460	/
S16_250_resi	$b/250$		432	−6.1%
S16_125_resi	$b/125$		428	−7.0%

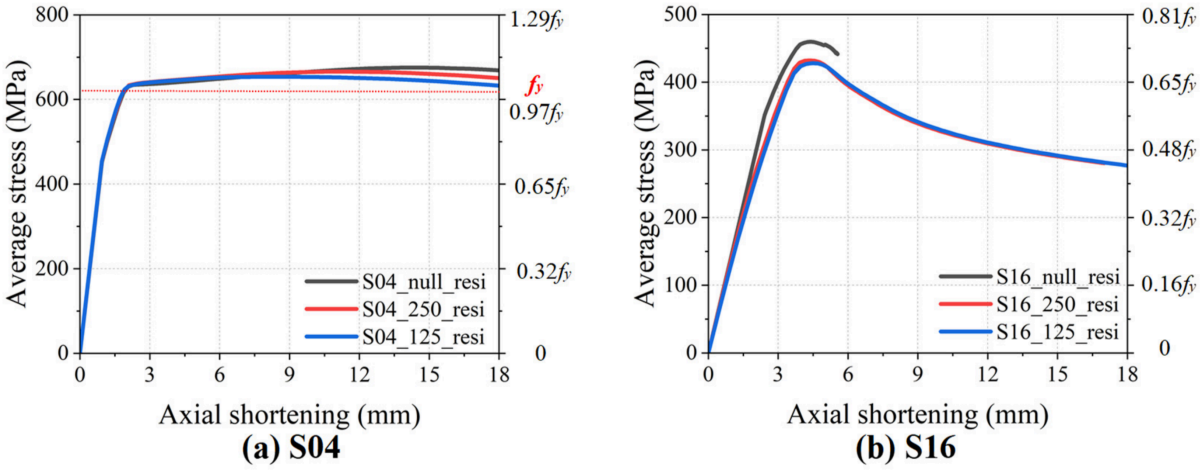


Figure 19. Average stress–axial shortening curves (effect of initial geometric imperfections).

4.4.2. Effect of Residual Stresses

As listed in Table 7, eight FE models were established to investigate the influence of residual stresses on the stiffened plates with and without initial imperfections, and the corresponding average stress–axial shortening curves obtained from the simulations are plotted in Figure 20. The results show that the inclusion of residual stresses reduces the overall stiffness of the stiffened plates when the average stress approaches the buckling strength. For specimen S04 with the smallest base-plate slenderness, the inclusion of residual stresses results in a slight increase in the buckling strength, with a maximum increase of 3.8%. In contrast, for specimen S16 with the largest base-plate slenderness, the buckling strength decreases slightly after considering residual stresses, with a maximum reduction of 6.5%. Overall, the effect of residual stresses on the buckling strength is limited.

Table 7. Comparison of buckling strengths (effect of residual stresses).

FE Model	Initial Geometric Imperfection	Residual Stress	Buckling Strength (MPa)	Difference in Buckling Strength
S04_null_null	null	null	662	/
S04_null_resi	null	As described in Section 4.1	675	2.0%
S04_125_null	$b/125$	null	630	/
S04_125_resi	$b/125$	As described in Section 4.1	654	3.8%
S16_null_null	null	null	492	/
S16_null_resi	null	As described in Section 4.1	460	−6.5%
S16_125_null	$b/125$	null	457	/
S16_125_resi	$b/125$	As described in Section 4.1	428	−6.3%

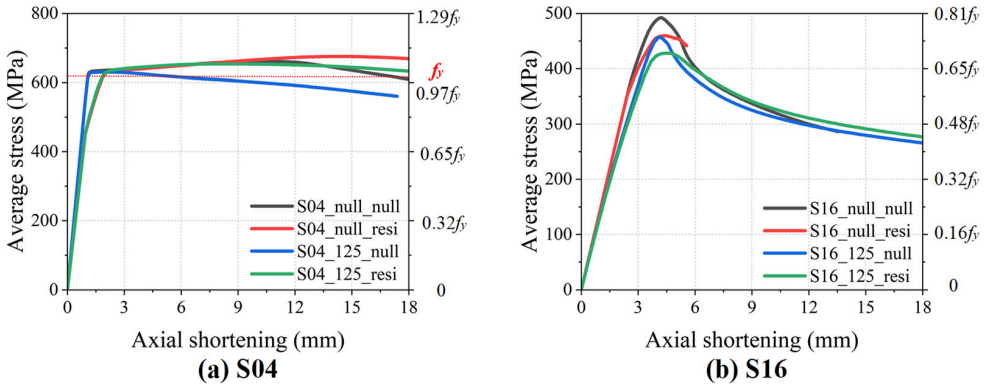


Figure 20. Average stress–axial shortening curves (effect of residual stresses).

4.4.3. Effect of Boundary Conditions

In the experiment, the two ends of the stiffened plates were unable to rotate freely, which is a rare strong constraint in practical structures. Therefore, for safety reasons, the rotational degrees of freedom (URX) at both ends of the stiffened plates in Figure 12 were released, and the impact of changes in the boundary conditions of stiffened plates on the buckling strength was analyzed. The amplitude of the initial imperfections used in the FE models was $b/125$, and the residual stress distribution described in Section 4.1 was applied. Four FE models were established, with the corresponding parameters shown in Table 8.

Table 8. Comparison of buckling strengths (effect of boundary conditions).

FE Model	Boundary Condition	Buckling Strength (MPa)	Difference in Buckling Strength
S04_fix	URX-limited	654	/
S04_rot	URX-free	638	−2.4%
S16_fix	URX-limited	428	/
S16_rot	URX-free	403	−5.8%

The simulation results are presented in Figure 21 and Table 8. It can be observed that releasing the rotational degree of freedom leads to a decrease in the buckling strength of the stiffened plates, with a maximum value of 5.8%, indicating that the changes in rotational degree of freedom has little effect on the buckling strength. However, Figure 21 shows that the change in rotational degree of freedom has an impact on the post-buckling behavior. When the rotational degree of freedom is released, the load-carrying capacity of the stiffened plate decreases more rapidly after buckling.

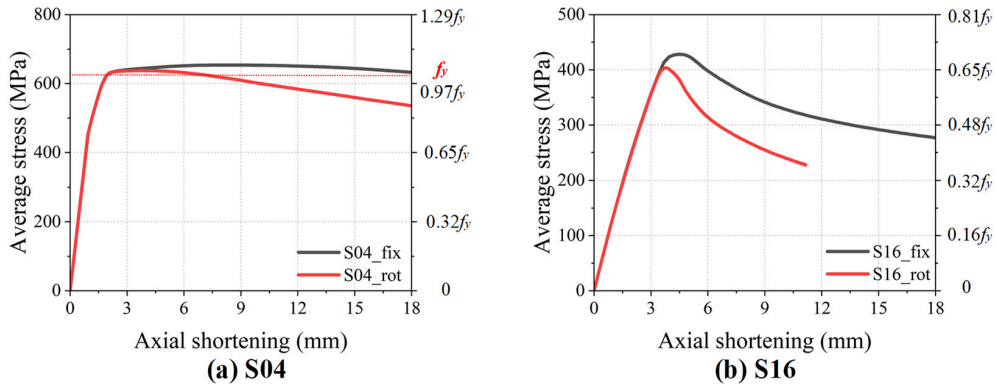


Figure 21. Average stress–axial shortening curves (effect of boundary conditions).

5. Evaluation of Current Design Codes

5.1. Current Design Codes

Based on the elastic buckling theory of plates, various national design codes primarily address local buckling issues by limiting the width-to-thickness ratio of plates, employing the effective section method, or introducing an allowable buckling strength reduction factor [10–12]. In these national design codes, the evaluation of the bearing capacity of stiffened plates considers not only the reduction factor for local buckling but also the influence of global instability.

5.1.1. Chinese Code

In the Chinese Specifications for Design of Highway Steel Bridges, the load-carrying capacity of stiffened plates P_u is computed as [10]:

$$P_u = \chi_{Ch} A_{eff,c} f_y \tag{4}$$

$$A_{eff,c} = \sum \rho_{Ch,loc} bt + \sum A_{st} \tag{5}$$

where χ_{Ch} refers to the global buckling reduction factor obtained from Equation (6); the local reduction factor $\rho_{Ch,loc}$ is related to plate slenderness and computed as Equation (9); t and b denote the thickness and width of the base plate unit; A_{st} denotes the rib area; f_y is the yield strength.

$$\chi_{Ch} = \begin{cases} 1 & \overline{\lambda}_{Ch} \le 0.2 \\ \frac{1}{2}\left\{1 + \frac{1}{\overline{\lambda}_{Ch}^2}(1+\varepsilon_{0g}) - \sqrt{\left[1 + \frac{1}{\overline{\lambda}_{Ch}^2}(1+\varepsilon_{0g})\right]^2 - \frac{4}{\overline{\lambda}_{Ch}^2}}\right\} & \overline{\lambda}_{Ch} > 0.2 \end{cases} \tag{6}$$

$$\varepsilon_{0g} = \alpha_g(\overline{\lambda}_{Ch} - 0.2) \tag{7}$$

$$\overline{\lambda}_{Ch} = \frac{\lambda_{Ch}}{\pi}\sqrt{\frac{f_y}{E}} \tag{8}$$

where λ_{Ch} represents the slenderness ratio of the stiffened plate; E is the Young's modulus; α_g is given as 0.5 for stiffened plates.

$$\rho_{Ch,loc} = \begin{cases} 1 & \overline{\lambda}_p \le 0.4 \\ \frac{1}{2}\left\{1 + \frac{1}{\overline{\lambda}_p^2}(1+\varepsilon_0) - \sqrt{\left[1 + \frac{1}{\overline{\lambda}_p^2}(1+\varepsilon_0)\right]^2 - \frac{4}{\overline{\lambda}_p^2}}\right\} & \overline{\lambda}_p > 0.4 \end{cases} \tag{9}$$

$$\varepsilon_0 = 0.8(\overline{\lambda}_p - 0.4) \tag{10}$$

where $\overline{\lambda}_p$ is the plate slenderness.

5.1.2. Eurocode

In Eurocode 3, the effective cross-section concept is adopted in the design of stiffened plates to account for local buckling effects [11]. The resistance of stiffened plates, P_u, is determined using Equation (11), in which both column-like and plate-like buckling behaviors are considered.

$$P_u = A_{c,eff} f_y \tag{11}$$

$$A_{c,eff} = \rho_{Eu,c} A_{c,eff,loc} + \sum b_{edge,eff} t \tag{12}$$

$$A_{c,eff,loc} = A_{sl,eff} + \sum_c \rho_{Eu,loc} b_{c,loc} t \tag{13}$$

where $\rho_{EUI,c}$ is the final reduction factor obtained from Equation (14), which is related to the effects of both column buckling behavior and plate buckling behavior; $A_{sl,eff}$ is the sum of the effective area of longitudinal stiffeners; the local reduction factor $\rho_{Eu,loc}$ is specified as Equations (17) and (18) which are for internal compression elements and outstand compression elements, respectively; $b_{edge,eff}$ is the width of the effective edge parts supported by adjacent plate elements, and $b_{c,loc}$ is the width of the base plate unit; t is the thickness of the base plate unit.

$$\rho_{Eu,c} = \chi_{Eu} + f(\rho - \chi_{Eu}) \tag{14}$$

$$\chi_{Eu} = \frac{1}{\Phi + \sqrt{\Phi^2 - \overline{\lambda}_{Eu}^2}} \tag{15}$$

$$\Phi = 0.5\left[1 + \alpha_e(\overline{\lambda}_{Eu} - 0.2) + \overline{\lambda}_{Eu}^2\right] \tag{16}$$

where χ_{Eu} is the reduction factor due to column buckling; $\overline{\lambda}_{Eu}$ is the relative column slenderness; α_e is the imperfection factor; f is the interpolation function for the determination of plate-like and column-like behavior; ρ is the reduction factor due to plate buckling.

$$\rho_{Eu,loc} = \begin{cases} 1 & \overline{\lambda}_p \le 0.5 + \sqrt{0.085 - 0.055\psi} \\ \frac{\overline{\lambda}_p - 0.055(3+\psi)}{\overline{\lambda}_p^2} & \overline{\lambda}_p > 0.5 + \sqrt{0.085 - 0.055\psi} \end{cases} \tag{17}$$

$$\rho_{Eu,loc} = \begin{cases} 1 & \overline{\lambda}_p \le 0.748 \\ \frac{\overline{\lambda}_p - 0.188}{\overline{\lambda}_p^2} & \overline{\lambda}_p > 0.748 \end{cases} \tag{18}$$

where Ψ denotes the stress ratio, and is 1.0 for uniform compression; $\overline{\lambda}_p$ is the plate slenderness.

5.1.3. Japanese Code

The Japanese Design Specifications of Highway Bridges address buckling within an allowable stress design framework [12]. The bearing capacity of stiffened plates is specified as:

$$P_u = \sigma_{cud} A_c \tag{19}$$

$$\sigma_{cud} = \rho_{Ja,crg}\rho_{Ja,loc} f_y \tag{20}$$

where $\rho_{Ja,crg}$ refers to the global buckling reduction factor obtained from Equation (21); $\rho_{Ja,loc}$ is the local buckling reduction factor and computed as Equation (23); f_y is the yield strength; A_c is the cross-section area.

$$\rho_{Ja,crg} = \begin{cases} 1 & \overline{\lambda}_{Ja} \le 0.2 \\ 1.109 - 0.545\overline{\lambda}_{Ja} & 0.2 < \overline{\lambda}_{Ja} \le 1.0 \\ \frac{1}{0.733 + \overline{\lambda}_{Ja}^2} & 1.0 < \overline{\lambda}_{Ja} \end{cases} \tag{21}$$

$$\overline{\lambda_{Ja}} = \frac{l}{\pi\sqrt{I/A_{nk}}}\sqrt{\frac{f_y}{E}} \tag{22}$$

where l denotes the effective length; I and A_{nk} are the second moment of area and the effective cross-sectional area, respectively; E is the Young's modulus; f_y is the yield strength.

$$\rho_{Ja,loc} = \begin{cases} 1 & \frac{R_R}{f_c} \leq 0.5 \\ 1.5 - \frac{R_R}{f_c} & 0.5 < \frac{R_R}{f_c} \leq 1.0 \\ 0.5\left(\frac{f_c}{R_R}\right)^2 & 1.0 < \frac{R_R}{f_c} \end{cases} \tag{23}$$

$$R_R = \left(\frac{B}{t}\right)\sqrt{\frac{12(1-\mu^2)f_y}{k_R E \pi^2}} = \overline{\lambda}_p \tag{24}$$

where f_y is the yield strength; B and t are the width and thickness of the base plate; μ is Poisson's ratio; E is the Young's modulus; $k_R = 4n^2$ denotes the buckling factor and n is the number of base plate units; f_c is the coefficient due to stress gradient and is 1.0 for uniform compression.

5.2. Evaluation

As mentioned above, national design codes assess the stability of stiffened plates by accounting for both the reduction factor due to local buckling and the influence of global buckling [10–12]. The objective of this study is to investigate the effect of local buckling of the base plate on the bearing capacity of stiffened plates. Therefore, to minimize the influence of global instability, additional parametric simulations were performed in this section based on the FE models validated in Section 4.2 by reducing the length L of the stiffened plate from $3b$ to b. In addition, as shown in Figure 11, the translational degree of freedom in the Z direction at the two side edges of the stiffened plate was constrained to simulate the lateral restraint provided by the angles, resulting in different base-plate slenderness values between the two side regions and the central region along the transverse direction. To eliminate this discrepancy, the widths of the two side base plate units were extended from $b/2$ to b, equal to those of the two central base plate units, and the translational degrees of freedom (UZ) at both side edges of the base plate were fully constrained.

Additionally, in design codes, the plate between the T-ribs of a stiffened plate is treated as being simply supported along all four edges. Section 4.4.3 shows that releasing the rotational degree of freedom in the X direction at both ends of the stiffened plate reduces its bearing capacity. Hence, the rotational degree of freedom in the X direction was released in these further parametric simulations. Furthermore, initial imperfections and residual stresses were considered, where the initial imperfection shape was taken as the first eigenmode from the modal analysis with an amplitude of $b/125$, and the residual stress distribution followed that described in Section 4.1. Finally, the yield strength is generally set as a reference value for evaluating the bearing capacity of the stiffened plate in the design codes. Therefore, the bilinear elastic-perfectly plastic model was adopted here, using the base-plate yield strength given in Table 1.

Considering all the above, a total of thirteen FE models were established, covering a true base-plate slenderness range from 0.44 to 1.74. The dimensional parameters of the stiffened plates in these FE models are summarized in Table 8. The true base-plate slenderness of stiffened plates in FE models S04_re, S07_re, S10_re, S13_re, and S16_re is the same as that of the specimens described in Section 2.2. For the stiffened plates with various dimensions listed in Table 9, the reduction factors accounting for global buckling effects on the bearing capacity χ_{Ch}, $\rho_{EU,c}$, and $\rho_{Ja,crg}$ were computed using Equations (6), (14), and (21), respectively. The corresponding values of the global buckling reduction factors, as shown in Table 9, are greater than 0.9 indicating that global buckling effects are relatively

minor. Hence, the isolated influence of local buckling can be reasonably investigated based on these FE models.

Table 9. Dimensional parameters of stiffened plates in FE models.

FE Model	Length L (mm)	Width of Base Plate Unit b (mm)	True Plate Slenderness	Reduction Factors for Global Buckling		
				Chinese Code χ_{Ch}	Eurocode $\rho_{EU,c}$	Japanese Code $\rho_{Ja,crg}$
S04_re	120	120	0.44	1.000	1.000	1.000
S05_re	140	140	0.51	1.000	1.000	1.000
S06_re	170	170	0.62	1.000	1.000	1.000
S07_re	210	210	0.76	1.000	1.000	1.000
S08_re	230	230	0.84	1.000	1.000	1.000
S09_re	260	260	0.94	1.000	1.000	1.000
S10_re	300	300	1.09	1.000	1.000	1.000
S11_re	310	310	1.13	0.996	1.000	0.996
S12_re	340	340	1.24	0.982	1.000	0.981
S13_re	390	390	1.42	0.958	0.992	0.956
S14_re	400	400	1.45	0.953	0.989	0.950
S15_re	420	420	1.53	0.942	0.981	0.939
S16_re	480	480	1.74	0.910	0.960	0.906

Based on the geometric parameters of the stiffened plates listed in Table 9, the buckling strength obtained from the FE analysis are presented in Figure 22, and it is evident that the buckling strength decreases continuously with increasing base-plate slenderness. Since the influence of global instability can be neglected, the local buckling reduction factors, namely $\rho_{Ch,loc}$, $\rho_{Eu,loc}$, and $\rho_{Ja,loc}$, were back-calculated from the FE-predicted buckling strengths using Equations (4), (11), and (19), respectively. These back-calculated values were compared with the values of $\rho_{Ch,loc}$, $\rho_{Eu,loc}$, and $\rho_{Ja,loc}$ directly determined from Equations (9), (17), and (23), as illustrated in Figure 23. The simulated values of $\rho_{Eu,loc}$ are close to the Eurocode predictions. However, for base-plate slenderness values of approximately 0.7–1.1, the Eurocode predictions are slightly higher than the simulated values of $\rho_{Eu,loc}$, indicating a slightly unconservative prediction of the local buckling of high-strength steel stiffened plates in this range. In comparison, the simulated values of the reduction factors $\rho_{Ch,loc}$ and $\rho_{Ja,loc}$ are significantly greater than those specified in the Chinese and Japanese codes, respectively, suggesting that both provisions are highly conservative.

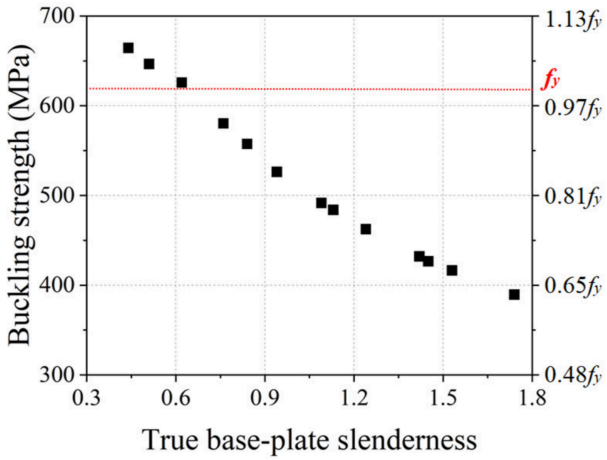


Figure 22. Comparison of buckling strengths from simulation results.

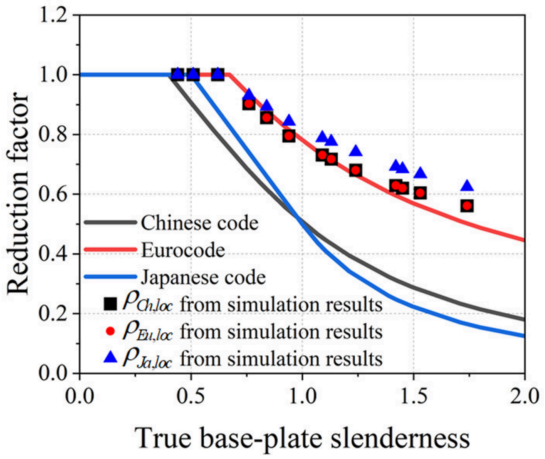


Figure 23. Comparison of reduction factors for local buckling.

In summary, the Eurocode provides approximate predictions, while the Chinese code and Japanese code provide conservative yet safe predictions for the reduction in bearing capacity of high-strength steel stiffened plates due to local buckling. However, the construction industry is highly material-consuming, energy-intensive, and cost-sensitive. Excessive conservatism in design codes, while ensuring safety, leads to uneconomic designs and is unfavorable to the pursuit of efficient and sustainable practices in the construction industry.

6. Conclusions

An experimental and numerical study on the local buckling behavior of the base plate in Q550 high-strength steel T-rib-stiffened plates was conducted. Five specimens were fabricated and tested under uniaxial compression. Initial geometric imperfections and residual stresses were measured and incorporated into FE simulations. A parametric study based on the validated FE models was performed to quantify the effects of residual stresses, geometric imperfections, and boundary conditions on the buckling behavior. The design methods in various national codes accounting for the local buckling behavior of stiffened plates were evaluated. Conclusions were drawn from the experimental and numerical results as follows:

(1) The failure processes of the stiffened plate specimens under compression can be roughly divided into three stages. Initially, the deformation is negligible and the axial compressive strain is uniformly distributed. Subsequently, local out-of-plane deformation develops in the base plate and increases with load, accompanied by significant diversions of axial strains near the deformed region, as well as deformation of the T-ribs to varying extents. In the final stage, the load decreases with increasing axial shortening, while the local out-of-plane deformation further intensifies and propagates, and the T-ribs exhibit varying degrees of in-plane and out-of-plane deformations. In addition, the buckling strength decreases with increasing base-plate slenderness.

(2) As the plate slenderness increases, the base plate becomes more susceptible to local buckling. The buckling behavior of stiffened plates transitions from plastic buckling to elastic buckling. When the plate slenderness rises from 0.44 to 1.74, the buckling strength decreases by approximately 36.7%. Additionally, numerical parametric analysis indicates that residual stresses have a limited effect on the buckling strength of the stiffened plates. For the stiffened plate with a base-plate slenderness of 1.74, the inclusion of residual stresses leads to a reduction in the buckling strength, with a

maximum decrease of 6.5%, whereas for a base-plate slenderness of 0.44, it increases by up to 3.8%.

(3) The initial geometric imperfections of high-strength steel stiffened plates primarily manifest as a protrusion on the base plate side, and the initial local imperfections of the base plate between adjacent T-ribs clearly exhibit a half-wave pattern. FE parametric simulations indicate that the buckling strength is moderately affected by the initial geometric imperfections. With an imperfection amplitude of $b/125$, the buckling strength of stiffened plates with a base-plate slenderness between 0.44 and 1.74 is reduced by up to 7.0%.

(4) When applying existing design codes to high-strength steel stiffened plates, the Eurocode provides approximate predictions for the local buckling strength, while the Chinese and Japanese design codes provide conservative yet safe predictions.

Author Contributions: P.C., writing—review and editing, writing—original draft, visualization, validation, methodology, investigation, formal analysis, data curation, conceptualization. Q.S., writing—review and editing, supervision, methodology. Y.L., writing—review and editing, methodology. S.W., writing—review and editing. Y.C., writing—editing. All authors have read and agreed to the published version of the manuscript.

Funding: This work was supported by the Science and Technology Commission of Shanghai Municipality (No. 23DZ1202305).

Data Availability Statement: Restrictions apply to the datasets.

Conflicts of Interest: Author Yongcheng Lu was employed by the company Shanghai Municipal Engineering Design Institute (Group) Co., Ltd. The remaining authors declare that the research was conducted in the absence of any commercial or financial relationships that could be construed as a potential conflict of interest.

References

1. He, X.; Wu, C.; Wang, R.; Wei, L.; Jiang, C. Experimental study on buckling behavior of orthotropic steel deck with slender open ribs for large span suspension bridges. *J. Constr. Steel Res.* **2023**, *201*, 107681. [CrossRef]
2. Chen, P.; Su, Q.; Ji, Y.; Zheng, B.; Su, H.; He, X. Experimental and numerical study on buckling behavior of curved stiffened plate for steel bridge towers. *Thin-Walled Struct.* **2025**, *227*, 114887. [CrossRef]
3. Jia, Y.; Ma, R.; Zhou, X.; Wang, B. The Buckling Behavior and Reliability Evaluation of a Cable-Stayed Bridge with Unique-Shaped Towers. *Materials* **2024**, *17*, 6124. [CrossRef] [PubMed]
4. Bonello, M.A.; Chryssanthopoulos, M.K.; Dowling, P.J. Ultimate strength design of stiffened plates under axial compression and bending. *Mar. Struct.* **1993**, *6*, 533–552. [CrossRef]
5. Bleich, F.; Ramsey, L.B.; Bleich, H.H. *Buckling Strength of Metal Structures*; McGraw-Hill Book Co., Ltd.: New York, NY, USA, 1952.
6. Somerville, W.L.; Swan, J.W.; Clarke, J.D. Measurement of residual stresses and distortions in stiffened panels. *J. Strain Anal. Eng. Des.* **1977**, *12*, 107–116. [CrossRef]
7. Nara, S.; Komatsu, S.; Kitada, T. A study on ultimate compressive strength properties of longitudinally stiffened continuous plates under uniaxial compression. *Doboku Gakkai Ronbunshu* **1988**, *1988*, 273–280. (In Japanese) [CrossRef]
8. Dow, R.S.; Smith, C.S. Effects of localized imperfections on compressive strength of long rectangular plates. *J. Constr. Steel Res.* **1984**, *4*, 51–76. [CrossRef]
9. Ueda, Y.; Yao, T. The influence of complex initial deflection modes on the behaviour and ultimate strength of rectangular plates in compression. *J. Constr. Steel Res.* **1985**, *5*, 265–302. [CrossRef]
10. *JTGD64-2015*; Specifications for Design of Highway Steel Bridges. Ministry of Transport of the People's Republic of China: Beijing, China, 2015.
11. *EN 1993-1-5*; Eurocode 3: Design of Steel Structures—Part 1-5: Plated Structural Elements. CEN: Brussels, Belgium, 2006.
12. Japan Road Association. *Design Specifications of Highway Bridges, Part II: Steel Bridges*; Japan Road Association: Tokyo, Japan, 2017.
13. Miki, C.; Homma, K.; Tominaga, T. High strength and high performance steels and their use in bridge structures. *J. Constr. Steel Res.* **2002**, *58*, 3–20. [CrossRef]
14. Shi, Y. Recent developments on high performance steel for buildings. *Adv. Struct. Eng.* **2012**, *15*, 1617–1622. [CrossRef]

15. Saufnay, L.; Demonceau, J.F. High-strength steels in steel structures: How to select the appropriate steel grade. *Structures* **2025**, *82*, 110820. [CrossRef]
16. Jiang, J.; Ye, Z.J.; Bao, W.; Wang, X.; Wang, Y.B.; Dai, X.H. Flexural buckling behaviour of 690 MPa high strength steel H-section columns. *Eng. Struct.* **2019**, *200*, 109718. [CrossRef]
17. Cao, X.; Zhao, G.; Kong, Z.; Shen, H.; Cheng, C.; Chen, Z.; Kim, S.-E. Experimental study on local buckling of 800 MPa HSS welded I-section columns under axial compression. *Thin-Walled Struct.* **2020**, *155*, 106878. [CrossRef]
18. Sun, L.; Han, Q.; Ye, M.; Jing, T.; Li, C. Post-local buckling behavior of welded high-strength steel box-section columns with ultra-thin plates. *Structures* **2025**, *80*, 110071. [CrossRef]
19. *EN 1993-2*; Eurocode 3: Design of Steel Structures—Part 2: Steel Bridges. CEN: Brussels, Belgium, 2006.
20. Wang, J.; Di, J.; Zhang, Q.; Qin, F.; Men, P. Local Buckling of Axially Compressed Welded H-Section Stub Columns Using Q420–Q960 Steel. *J. Struct. Eng.* **2023**, *149*, 04023119. [CrossRef]
21. Wang, J.; Di, J.; Zhang, Q.; Qin, F. Overall buckling behaviour of Q420–Q960 steel welded H-section axial compression members. *Eng. Struct.* **2021**, *249*, 113340. [CrossRef]
22. Zheng, H.; Cai, L.; Qin, J.; Mi, Y.; Jiang, L.; Ma, X.; Sun, Z. Lateral performance analysis of trapezoidal orthogonal stiffened steel plate shear walls. *Buildings* **2024**, *14*, 1634. [CrossRef]
23. Wang, F.; Cai, Y.; Ma, Z.; Xu, A.; Zhang, H.; Ji, C.; Ren, S. Effect of aspect ratio and geometric defects on the stability performance of U-rib stiffened plates. *Structures* **2024**, *68*, 107082. [CrossRef]
24. Chou, C.C.; Uang, C.M.; Seible, F. Experimental Evaluation of Compressive Behavior of Orthotropic Steel Plates for the New San Francisco–Oakland Bay Bridge. *J. Bridge Eng.* **2006**, *11*, 140–150. [CrossRef]
25. Choi, B.; Hwang, M.; Yoon, T.; Yoo, C. Experimental study of inelastic buckling strength and stiffness requirements for longitudinally stiffened panels. *Eng. Struct.* **2009**, *31*, 1141–1153. [CrossRef]
26. Sadamoto, S.; Tanaka, S.; Taniguchi, K.; Ozdemir, M.; Bui, T.; Murakami, C.; Yanagihara, D. Buckling analysis of stiffened plate structures by an improved meshfree flat shell formulation. *Thin-Walled Struct.* **2017**, *117*, 303–313. [CrossRef]
27. Jiang, H. *Study on the Stability Performance and Design Method of High Strength Steel Stiffened Plates Under Axial Compression*; Chongqing University: Chongqing, China, 2020.
28. Li, S.; Kim, D.K.; Benson, S. The influence of residual stress on the ultimate strength of longitudinally compressed stiffened panels. *Ocean Eng.* **2021**, *231*, 108839. [CrossRef]
29. Yi, M.S.; Noh, S.H.; Lee, D.H.; Seo, D.H.; Paik, J.K. Direct measurements, numerical predictions and simple formula estimations of welding-induced biaxial residual stresses in a full-scale steel stiffened plate structure. *Structures* **2021**, *29*, 2094–2105. [CrossRef]
30. Wang, S.; Su, Q.; Jiang, X.; Ghafoori, E. Stability of steel columns with bolted strengthening under preload: Experimental study. *J. Constr. Steel Res.* **2022**, *190*, 107119. [CrossRef]
31. He, X.; Wu, C.; Wang, R.; Wei, L.; Jiang, C. Buckling behavior of orthotropic steel deck stiffened by slender bulb flats for large span bridges. *Thin-Walled Struct.* **2023**, *188*, 110797. [CrossRef]
32. Faulkner, D. A review of effective plating for use in the analysis of stiffened plating in bending and compression. *J. Ship Res.* **1975**, *19*, 1–17. [CrossRef]
33. Khan, I.; Zhang, S. Effects of welding-induced residual stress on ultimate strength of plates and stiffened panels. *Ships Offshore Struct.* **2011**, *6*, 297–309. [CrossRef]
34. Chen, J. Experimental and Numerical Simulation Study of Welding Residual Stress in Stiffened Plate with Open Ribs. Master's Thesis, Fuzhou University, Fuzhou, China, 2018.
35. Lima, J.P.S.; Cunha, M.L.; dos Santos, E.D.; Rocha, L.A.O.; de Vasconcellos Real, M.; Isoldi, L.A. Constructal Design for the ultimate buckling stress improvement of stiffened plates submitted to uniaxial compressive load. *Eng. Struct.* **2020**, *203*, 109883. [CrossRef]
36. Yun, X.; Zhu, Y.; Meng, X.; Gardner, L. Welded steel I-section columns: Residual stresses, testing, simulation and design. *Eng. Struct.* **2023**, *282*, 115631. [CrossRef]
37. Benson, S.; Downes, J.; Dow, R.S. An automated finite element methodology for hull girder progressive collapse analysis. In Proceedings of the 11th International Marine Design Conference, Glasgow, UK, 10–13 June 2012.
38. *BS EN 1090-2:2018*; Execution of Steel Structures and Aluminium Structures—Part 2: Technical Requirements for Steel Structures. CEN: Brussels, Belgium, 2018.
39. *JTG/T 3651-2022*; Specification for Manufacture and Installation of Highway Steel Bridge. Ministry of Transport of the People's Republic of China: Beijing, China, 2022.

Disclaimer/Publisher's Note: The statements, opinions and data contained in all publications are solely those of the individual author(s) and contributor(s) and not of MDPI and/or the editor(s). MDPI and/or the editor(s) disclaim responsibility for any injury to people or property resulting from any ideas, methods, instructions or products referred to in the content.